J. Fluid Mech. (2023), *vol*. 965, A8, doi:10.1017/jfm.2023.395

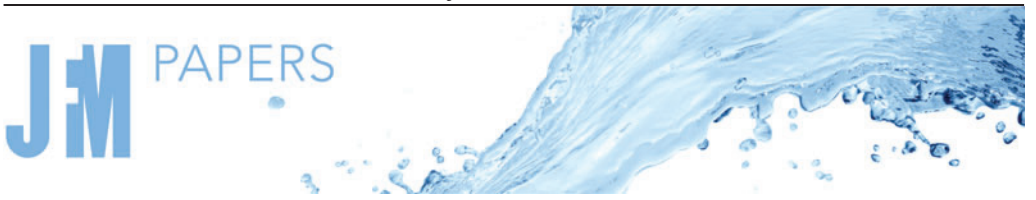

Convergent Richtmyer–Meshkov instability on two-dimensional dual-mode interfaces

Jinru Xu[1], **He Wang**[1], **Zhigang Zhai**[1,†] **and Xisheng Luo**[1,†]

[1]Advanced Propulsion Laboratory, Department of Modern Mechanics, University of Science and Technology of China, Hefei 230026, PR China

(Received 25 December 2022; revised 4 May 2023; accepted 5 May 2023)

We report the first shock-tube experiments on two-dimensional dual-mode air–SF_6 interfaces with different initial spectra subjected to a convergent shock wave. The convergent shock tube is specially designed with a tail opening to highlight the Bell–Plesset (BP) and mode-coupling effects on amplitude development of fundamental mode (FM). The results show that the BP effect promotes the occurrence of mode coupling, and the feedback of high-order modes to the FM also arises earlier in convergent geometry than that in its planar counterpart. Relatively, the amplitude growth of the FM with a higher mode number is inhibited by the feedback, and saturates earlier. The FM with a lower mode number is affected more heavily by the BP effect, and finally dominates the flow. A new model is proposed to well predict the amplitude growths of the FM and high-order modes in convergent geometry. In particular, for FM that reaches its saturation amplitude, the post-saturation relation is introduced in the model to achieve a better prediction.

Key words: shock waves

1. Introduction

The impulsive acceleration of a perturbed interface separating fluids of different densities, typically due to a shock wave traversing the interface, results in the growth of interfacial perturbations. This instability was first studied theoretically by Richtmyer (1960) and later experimentally by Meshkov (1969). It is therefore known as the Richtmyer–Meshkov (RM) instability. The RM instability development is generally driven by baroclinic vorticity produced on the interface due to misalignment of the pressure gradient (provided by the shock wave) and density gradient between the two materials. The perturbation amplitude grows linearly at the early stage under certain conditions. When these conditions are not satisfied, the amplitude exhibits nonlinear growth and, given sufficient initial

† Email addresses for correspondence: sanjing@ustc.edu.cn, xluo@ustc.edu.cn

energy, eventually the flow transitions to a turbulent mixing state. The RM instability is an important phenomenon occurring in many applications. For example, in inertial confinement fusion (ICF) reactions, the mixing induced by the RM instability (created by surface non-uniformities at the fuel–shell interface or by non-uniform radiation drive) results in the contamination of the fuel and limits the fusion energy gain (Lindl *et al.* 2014; Chu *et al.* 2022). An understanding of the various stages of these instabilities is an essential requirement of ICF efforts. In supersonic combustion, the RM instability increases the mixing between the fuel and oxidizer, enhancing combustion efficiency (Yang, Kubota & Zukoski 1993). A better understanding of the RM instability could allow for improved design of combustors that optimizes mixing for combustion.

In previous studies, a single-mode interface has been widely used to investigate the RM instability because of its simple configuration. Experimentally, the single-mode interface was created by using the nitrocellulose membrane technique (Meshkov 1969; Jourdan & Houas 2005), membrane-less technique (Jacobs 1992; Jacobs *et al.* 1993, 1995; Balakumar *et al.* 2012; Morgan *et al.* 2012; Vandenboomgaerde *et al.* 2014) or soap-film technique (Luo, Wang & Si 2013; Liu *et al.* 2018), and the shocked interface behaviours have been thoroughly studied. Theoretically, various single-mode models for different evolution stages based on several assumptions have been proposed, e.g. models for the linear stage (Richtmyer 1960; Meyer & Blewett 1972; Wouchuk 2001; Luo *et al.* 2013), early nonlinear stage (Zhang & Sohn 1996, 1997; Mariani *et al.* 2008) and late nonlinear stage (Goncharov 2002; Sohn 2003; Jacobs & Krivets 2005).

In practical applications, however, random multi-mode perturbations commonly exist on initial interfaces. After a shock wave acceleration, complicated mechanisms, such as high-order harmonic generation and bubble merger process (Sadot *et al.* 1998; Niederhaus & Jacobs 2003; Leinov *et al.* 2009; Orlicz, Balasubramanian & Prestridge 2013; Pandian, Stellingwerf & Abarzhi 2017; Elbaz & Shvarts 2018; Mohaghar *et al.* 2019), are generally involved. Previous studies have shown that in the multi-mode RM instability, each mode develops independently at the linear stage. When the mode amplitude develops comparable to its wavelength, the evolution enters the nonlinear stage, and mode coupling becomes very significant (Haan 1989, 1991; Ofer *et al.* 1996). Finally, under the assumption that there are no longer any larger-wavelength perturbations yet to saturate, the interface development enters the bubble merging stage, where smaller bubbles are gradually swallowed up by larger bubbles (Alon *et al.* 1995; Sadot *et al.* 1998; Guo *et al.* 2019).

Experiments of a dual-mode RM instability under high-Mach-number conditions have been performed (Di Stefano *et al.* 2015*a*,*b*), and the results indicated that new modes are generated from mode coupling, and their amplitudes grow and saturate over time. The dual-/multi-mode RM instability under weak shock conditions in planar geometry was also investigated to explore the dependence of interface development on its initial shape (Luo *et al.* 2020; Liang *et al.* 2021*a*). The growth rate of the multi-mode RM instability was found to strongly rely on the wavenumber, phase and amplitude of initial constituent modes. The interaction of a small-wavelength multi-mode perturbation with a large-wavelength inclined interface perturbation was investigated using three-dimensional (3-D) simulations (McFarland *et al.* 2015). It was shown that the flow has a distinct memory of the initial conditions that are present in both large-scale-driven entrainment measures and small-scale-driven mixing measures. A similar conclusion was also drawn by Mohaghar *et al.* (2017) in their experimental work using density and velocity statistics. Further, the effect of initial perturbations on the evolution of the inclined RM turbulent mixing layer was investigated by Mohaghar, McFarland & Ranjan (2022) through 3-D simulations. The results indicated that the multi-mode perturbations produce a completely different mixing mechanism compared with the single-mode case.

Compared with the planar RM instability, the convergent RM instability is more closely related to ICF. In the convergent RM instability, both radial and angular directions are involved, and the perturbation development is associated with more mechanisms. Bell (1951) and Plesset (1954) first analysed the early-time growth of the Rayleigh–Taylor (RT) instability (Rayleigh 1883; Taylor 1950) in cylindrical and spherical geometries, and found that the perturbation growth rate varies with interface radius, referred to as the Bell–Plesset (BP) effect. Several nonlinear models (Mikaelian 2005*b*; Liu, He & Yu 2012; Liu *et al.* 2014; Wang *et al.* 2015) revealed that the BP effect suppresses nonlinearity and extends the linear stage longer than that in the planar configuration, as demonstrated in laser-driven experiments (Fincke *et al.* 2005). Besides, for continuous radial flow behind a convergent shock, the interface as a whole is in a non-uniform pressure field, which inevitably introduces the RT effect (Lanier *et al.* 2003; Lombardini, Pullin & Meiron 2014; Ding *et al.* 2017; Samulski *et al.* 2022). Therefore, coupling of the BP effect, RT effect and multiple impacts (shocks reflected back and forth between the interface and convergence centre) greatly increases the complexity of the convergent RM instability.

Experimental measurements of single-mode perturbation amplitude in the convergent RM instability were performed by Ding *et al.* (2017), and the RT stabilization caused by interface deceleration was found to reduce the growth rate. By reasonably evaluating the RT stabilization, a modified model based on the Bell equation was proposed to predict the perturbation growth before reshock. Luo *et al.* (2018) found that the long-term effect of the RT stabilization even leads to a phase inversion on the single-mode light–heavy interface before reshock provided that the initial interface has sufficiently small perturbations. Further, Zhai *et al.* (2019) numerically investigated the RT effect on the phase inversion observed in experiments (Luo *et al.* 2018), considering effects of the initial amplitude, azimuthal mode number and reshock timing. A novel shock tube was designed to study the nonlinear features of the convergent single-mode RM instability (Luo *et al.* 2019). The shock tube employs a concave–oblique–convex wall profile which first transforms a planar shock into a cylindrical arc, then gradually strengthens the cylindrical shock along the oblique wall and finally converts it back into a planar one. Therefore, the new facility can realize the analysis of nonlinearity of the convergent RM instability by eliminating the RT effect and reshock. The perturbation amplitude experiences a linear growth much longer than that in planar geometry, which is mainly ascribed to the counteraction between the promotion by the BP effect and the suppression by nonlinearity.

Previous studies associated with the convergent RM instability mainly focused on the development of a single-mode perturbation. However, the interaction of a convergent shock with multi-mode interfaces is more relevant to ICF. Relative to the convergent single-mode RM instability, mode-coupling effects are introduced in the convergent multi-mode RM instability. Kumar, Hornung & Sturtevant (2003) studied the growth of a multi-mode initial interface, formed by sandwiching a polymeric membrane between wire-mesh frames, in a conical geometry, and found that the turbulent mixing zone has a relatively larger growth rate than that in the planar counterpart. Mode coupling in the convergent RM instability of a dual-mode interface has been numerically investigated by Zhou *et al.* (2020). The first-mode amplitude growth was found to depend heavily on the second mode, and the amplitude signs of harmonics generated for all possible dual-mode configurations were obtained. Besides, the second-order weakly nonlinear solutions for a dual-mode interface subjected to a uniformly radical motion, i.e. a pure BP environment, were obtained by Guo, Cheng & Li (2020). Until now, experiments related to the convergent multi-mode RM instability have been scarce mainly because a uniformly convergent shock and a well-defined initial interface are difficult to generate in experiments and

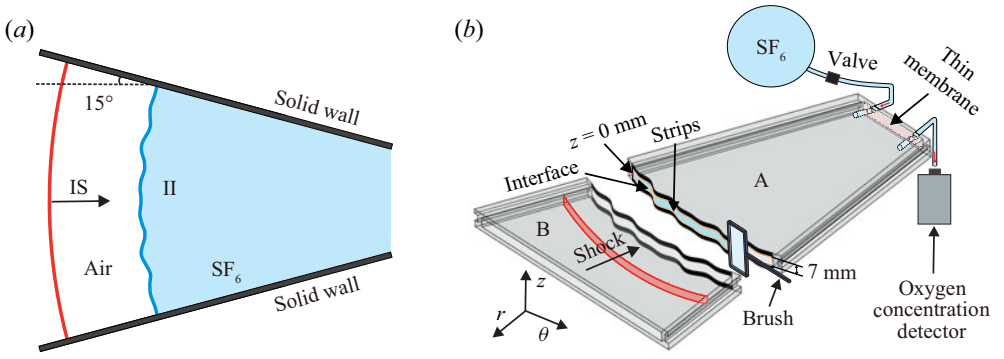

Figure 1. Sketches of a convergent shock interacting with a dual-mode interface (*a*) and of the interface formation process (*b*). IS, incident convergent shock; II, initial interface.

complicated mechanisms are involved. In our previous work, a smoothly convergent shock was generated based on shock dynamics theory (Zhai *et al.* 2010; Zhan *et al.* 2018; Luo *et al.* 2019), and a well-defined initial multi-mode interface was formed by the soap-film technique (Liang *et al.* 2021*a*; Guo *et al.* 2022). These provide us an opportunity to explore the developments of multi-mode interfaces accelerated by a convergent shock.

In the convergent RM instability, the BP effect always exists. During the coasting stage of an ICF implosion (Craxton *et al.* 2015), the shell moves at a constant velocity, which means that perturbations on the shell evolve in an approximately pure BP environment. Therefore, it is necessary to explore the pure BP growth of multi-mode perturbations. However, the RT effect, BP effect, mode coupling and reshock are generally coupled together, and it is difficult to decouple them. It is unclear as to how the BP effect and mode coupling behave in the convergent multi-mode RM instability. Starting from a simple configuration, i.e. a dual-mode interface, interaction of a convergent shock with a dual-mode air–SF_6 interface is experimentally investigated in this work. The experiments are conducted in the same convergent shock tube as that used by Luo *et al.* (2019). In this convergent shock tube, the RT effect and reshock are avoided, and compressibility is also negligible. Therefore, the BP and mode-coupling effects can be highlighted. Six kinds of dual-mode air–SF_6 interfaces with different initial perturbation spectra are formed to explore the dependency of shocked flow on initial conditions. The objectives of present work are twofold. The first is to evaluate the mode-coupling effects on the growth rate of each mode in convergent geometry. The second is to demonstrate the different roles of the BP effect and mode coupling in dual-mode perturbation developments.

In the following, the experimental methods are first provided. Then, the flow features are qualitatively described and the mode amplitude growth for each dual-mode case is presented and compared with the single-mode counterpart to highlight the mode-coupling effects. Finally, the predictions of the mode amplitude growth are presented to evaluate the BP effect.

2. Experimental methods

The dual-mode interface, as sketched in figure 1(*a*), is superimposed by two cosine perturbations: $r(\theta) = R_0 + a_0 \cos(m_1\theta + \phi_1) + a_0 \cos(m_2\theta + \phi_2)$, where $R_0 = 270$ mm refers to the mean radius of initial interface, $a_0 = 1.0$ mm is the initial amplitude of

each fundamental mode, m_i $(i = 1, 2)$ is the azimuthal mode number and ϕ_i $(i = 1, 2)$ is the initial phase. The dual-mode interfaces can be divided into two groups based on the phase difference between fundamental modes: in-phase and anti-phase. Each group includes three mode combinations: $(m_1, m_2) = (48, 24)$, (72, 24) and (72, 48). Therefore, the effects of relative phase and mode combination on the shocked dual-mode interface evolution can be studied. To facilitate comparison and to obtain the background flow field, three single-mode cases corresponding to the three fundamental modes involved and one undisturbed case are also considered. The detailed initial conditions for each dual-mode case (denoted by relative phase m_1–m_2) and each single-mode case (denoted by SM m) are listed in table 1.

The soap-film technique (Luo *et al.* 2016; Liang *et al.* 2021*a*; Guo *et al.* 2022) is used to form the well-defined dual-mode interfaces. Before interface formation, the transparent devices (devices A and B) shown in figure 1(*b*) are manufactured by combining two transparent acrylic plates (3.0 mm in thickness) with pedestals (7.0 mm in height). Two identical constraint strips (0.50 mm in width and 0.25 mm in thickness) are attached to the pre-carved grooves on device A to constrain the soap film. The ratio of the total height of the constraint strips protruding into the flow field to the height of the whole flow field is smaller than 10 %, and thus the constraint strips have negligible effects on the shocked flow (Wang *et al.* 2022). To generate the soap-film interface, the constraint strips are wetted by the soap solution (78 % pure water, 2 % sodium oleate and 20 % glycerin by mass) in advance, then a rectangular brush with the soap solution attached is pulled carefully along the constraint strips and finally the soap-film interface is generated.

To create an air–SF_6 interface, air in device A needs to be replaced by SF_6. As illustrated in figure 1(*b*), a thin membrane is used to seal device A, and two pipes are inserted into device A through the membrane. The SF_6 is injected into device A through the inlet pipe and air is exhausted through the outlet pipe. An oxygen concentration detector is placed at the outlet pipe to monitor the oxygen concentration in device A. Once the volume fraction of oxygen is reduced to less than 0.5 %, the pipes and thin membrane are removed to avoid shock reflection, and experiments are conducted immediately. The time interval is short enough and will not introduce additional uncertainty of gas concentration (Luo *et al.* 2019). According to one-dimensional gas dynamics theory, the gas components on both sides of the interface, as listed in table 1, are determined by velocities of the incident and transmitted shock waves measured from experimental schlieren images.

Experiments are conducted in a convergent shock tube with a smooth concave–oblique–convex wall designed to modify the shock shape (Luo *et al.* 2019; Li *et al.* 2020). The present design enables a strong convergent shock near the convergence centre to exit the convergent section without shock focusing and reflecting. Thus, interface deceleration and reshock are eliminated, and contributions from the BP effect and mode coupling to the perturbation growth are isolated. The postshock flow is recorded by high-speed schlieren photography. The frame rate of the camera (FASTCAM SA-Z, Photron Limited) is 50 400 frames per second, and the spatial resolution of each image is 0.285 mm pixel^{-1}. The ambient pressure and temperature are 101.3 ± 0.1 kPa and 294.7 ± 2 K, respectively. The Mach number of the convergent shock just before it meets the interface is $M_s = 1.26 \pm 0.01$.

Before performing the experiments, the boundary-layer effect is first evaluated. It is found from the schlieren images that no obvious turbulence characteristics appear on the evolving interface. In addition, the Reynolds numbers (Re) at four moments are discussed here. Note that the calculation methods of Re almost involve the vorticity field information, which is unable to be obtained in the present experiments. In this work, Re for the RM

https://doi.org/10.1017/jfm.2023.395 Published online by Cambridge University Press

Case	m_1	m_2	ϕ_1	ϕ_2	λ_{m_1}	λ_{m_2}	a_0/λ_{m_1}	a_0/λ_{m_2}	A^+	ψ	v_i	Δv	v_f	v_t
I48-24	48	24	0	0	35.343	70.686	0.028	0.014	−0.67	0.97	430.9	93.4	258.5	201.1
I72-24	72	24	0	0	23.562	70.686	0.042	0.014	−0.67	0.97	430.9	93.4	258.5	201.1
I72-48	72	48	0	0	23.562	35.343	0.042	0.028	−0.67	0.97	431.0	90.0	258.6	201.1
A48-24	48	24	π	0	35.343	70.686	0.028	0.014	−0.67	0.98	430.4	93.3	258.3	200.9
A72-24	72	24	π	0	23.562	70.686	0.042	0.014	−0.67	0.98	431.0	94.8	262.9	198.2
A72-48	72	48	π	0	23.562	35.343	0.042	0.028	−0.67	0.97	431.0	93.4	258.6	201.1
SM 24	24	—	0	—	70.686	—	0.014	—	−0.67	0.97	430.9	93.4	258.4	196.8
SM 48	48	—	0	—	35.343	—	0.028	—	−0.68	0.98	430.7	90.4	258.4	201.0
SM 72	72	—	0	—	23.562	—	0.042	—	−0.67	0.97	430.9	93.4	258.5	201.1

Table 1. Initial conditions of dual- and single-mode interfaces studied in the present work. Here, m_i, ϕ_i, a_0/λ_{m_i} $(i = 1, 2)$ refer to the initial mode number, phase and amplitude–wavelength ratio of the corresponding constituent mode, respectively; A^+ is the post-shock Atwood number $(A^+ = (\rho_2^+ - \rho_1^+)/(\rho_2^+ + \rho_1^+)$ with ρ_2^+ and ρ_1^+ being the post-shock densities of air and SF_6); ψ is the SF_6 mass fraction on the downstream side of the interface; v_i is the the velocity of the incident convergent shock just before it meets the interface; Δv is the the interface velocity jump by shock impact; v_f is the reflected shock velocity; and v_t is the transmitted shock velocity. The units for length and velocity are mm and m s^{-1}, respectively.

Times	0.1 ms	0.4 ms	0.7 ms	1.0 ms
Re	6.8×10^3	8.4×10^3	8.9×10^3	9.1×10^3

Table 2. The values of Reynolds number at different moments.

Models	$\delta = 4.9\sqrt{\frac{\mu r_m}{\rho \Delta v}}$	$\delta^* = 1.72\sqrt{\frac{\mu r_m}{\rho \Delta v}}$	$\delta^{**} = 0.664\sqrt{\frac{\mu r_m}{\rho \Delta v}}$
Air	0.63 mm	0.22 mm	0.09 mm
SF_6	0.28 mm	0.10 mm	0.04 mm

Table 3. The boundary-layer thickness calculated from different laminar models.

instability turbulence is calculated, trying to give a rough judgement on whether there is a transition. The Reynolds number is calculated by $Re = h\dot{h}/\nu_{mix}$, where h is half of the mixing width, $\dot{h}$ is the growth rate of h and ν_{mix} is the mixing kinematic viscosity of the two gases. The mixing kinematic viscosity can be obtained by using $(\mu_1 + \mu_2)/(\rho_1 + \rho_2)$, where μ_1 and μ_2 (ρ_1 and ρ_2) are the viscosities (densities) of the mixed gases at the left and right sides of the interface, respectively (Mohaghar *et al.* 2017; Guo *et al.* 2022). According to one-dimensional gas dynamics theory, ν_{mix} is calculated as 2.79×10^{-6}. The values of *Re* at four moments are given in table 2. As stated by Dimotakis (2000), achieving $Re \sim 10^4$ is conjectured to be necessary to observe a mixing transition and is a more restrictive condition beyond conditions for turbulent transition. However, the Reynolds numbers in our experiments have not yet developed to meet the necessary conditions for a mixing transition. As a result, a laminar model is suitable for calculating the boundary-layer thickness in our experiments. In this work, three laminar models are used to calculate the boundary-layer thickness, and their expressions are given in table 3. In this table, $r_m = 100$ mm refers to the maximum distance that the interface moves in the radial direction, $\rho = 1.204$ kg m^{-3} ($\rho = 6.143$ kg m^{-3}) and $\mu = 1.83 \times 10^{-5}$ Pa s ($\mu = 1.6 \times 10^{-5}$ Pa s) are the density and viscosity coefficient of pure air (SF_6), respectively, and $\Delta v = 93.4$ m s^{-1} represents the postshock flow velocity. The results calculated show that the boundary-layer thickness during the time studied is much smaller than the inner height of the test section (7.0 mm), and it has a limited effect on the interface movements.

Then any 3-D effects of the soap-film interface are evaluated. Taking case I72-24 as an example, the interface amplitudes at the boundary slice ($z = \pm 3.5$ mm) and symmetry slice ($z = 0$ mm) are 2.0 and 1.907 mm according to previous work (Luo *et al.* 2013; Liang *et al.* 2021*b*). The absolute difference between these two amplitudes is 0.093 mm, which is much smaller than the size of a single pixel in the schlieren images. Therefore, 3-D effects may be considered negligible.

3. Results and discussion

3.1. *Interface morphologies and flow features*

Developments of the unperturbed and single-mode interfaces are similar to those in the work of Luo *et al.* (2019) and, therefore, the related descriptions are omitted. Distinct schlieren images showing developments of the in-phase dual-mode interfaces are presented in figure 2. The time origin ($t = 0$ μs) is defined as the moment when the IS

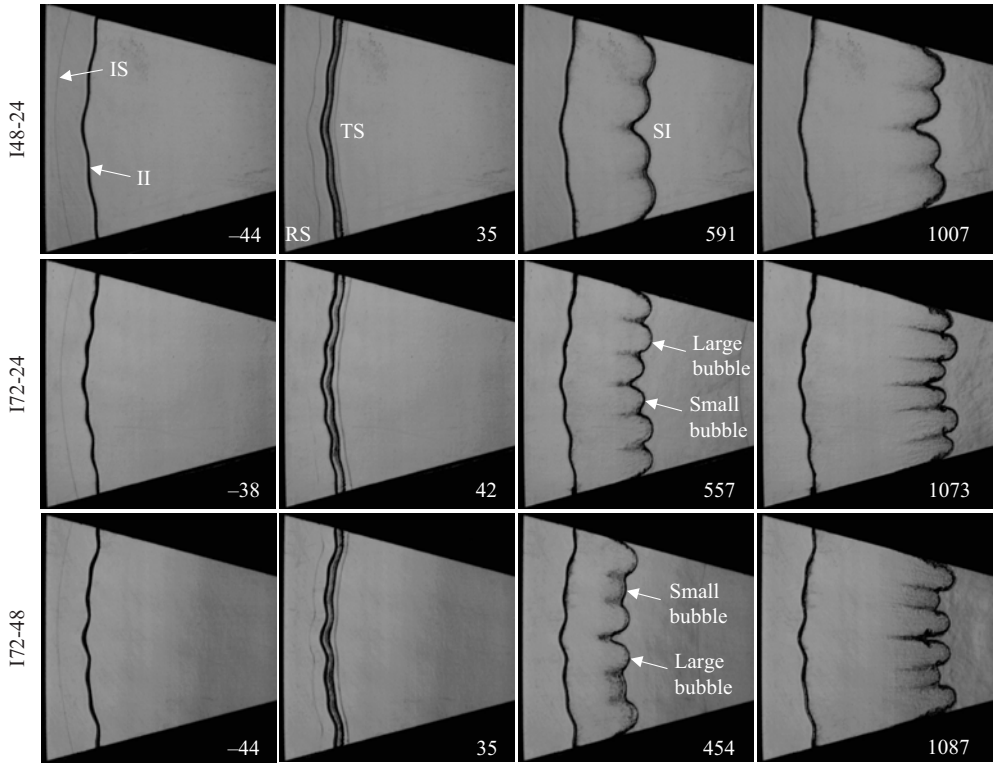

Figure 2. Experimental schlieren images illustrating the in-phase dual-mode interface evolution. RS, reflected shock; TS, transmitted shock; SI, shocked interface. Other symbols have the same meaning as those in figure 1. Numbers denote the time in μs.

arrives at the average position of the II, i.e. $r = R_0$. Taking case I48-24 as an example, before IS impact ($t = -44\mu s$), the interface profile looks quite thick because the interface in the schlieren image is covered by two dual-mode strips. When IS passes across II, it bifurcates into a downstream-moving TS and an upstream-propagating RS ($t = 35$ μs). The SI leaves its original location, and its profile is thin and clean. This indicates that the diffusion layer (Jacobs & Krivets 2005) and three-dimensionality (Luo *et al.* 2018) of the interface are greatly reduced. At early times, the interface is still single-valued and the shape of the original perturbation is visible. As time proceeds, the perturbation width, defined as the difference between the maximum and minimum radii of the points on the interface in the radial direction, increases continuously. Eventually, finger-like bubbles (lighter fluid penetrating into heavier fluid) and spikes (heavier fluid penetrating into lighter fluid) arise ($t = 591$–1007 μs) due to increasing nonlinearity. In this case, no prominent vortices arise during the time studied, and four nearly equal bubbles occupy the flow.

For the other two cases, some spikes start to roll up with a pair of vortices formed on their necks ($t = 1073$ μs in case I72-24 for example), causing the interface to become multi-valued. In case I72-24, there are two large bubbles and four small bubbles, and an arrangement of a large bubble with two small bubbles on both sides is observed. In case I72-48, there are four large bubbles and two small bubbles, and an arrangement of a small bubble with two large bubbles on both sides is observed. Spikes between the large and small bubbles skew towards the large bubbles, which is indicative of the bubble merger

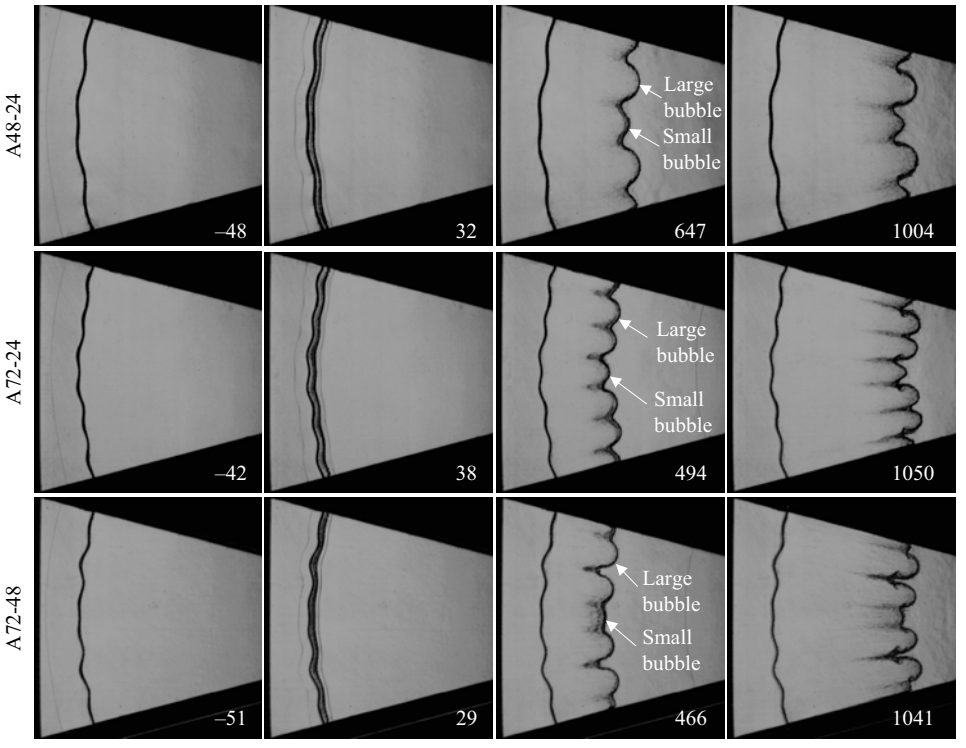

Figure 3. Schlieren images illustrating the anti-phase dual-mode interface evolution.

process (Sadot *et al.* 1998; Alon *et al.* 1994, 1995). The flow diversity demonstrates that the initial mode combination significantly affects the perturbation morphology. As spikes grow, they seem to be dragged. As discussed earlier, the boundary-layer effect can be neglected. Actually, the spikes move forward followed by the soap-film droplets. After the shock wave impact, the soap film breaks into small droplets immediately. These droplets cannot catch up with the high-speed flow, which leads to the black lines along the line of sight in the schlieren images. The relationship between the size of the soap droplets and the shock strength was investigated by Ranjan *et al.* (2008) and Cohen (1991). According to their work, the mean radius of the soap droplets is estimated to be 30 μm for the shock with $M_s \sim 1.3$. Moreover, Liang *et al.* (2019) investigated the interaction of a planar air–SF_6 interface with a planar shock, and found a negligible effect of the soap droplets on the interface motion.

Figure 3 shows developments of the anti-phase dual-mode interfaces. In case A48-24, large bubble and small bubble are arranged alternately, and again no prominent vortices arise ($t = 1004\mu$s). In case A72-24 , the flow is occupied by four large bubbles and a small bubble, and four large bubbles are distributed symmetrically on both sides of the small bubble ($t = 1050$ μs). Spikes between the two large bubbles are less prominent than those between the large and small bubbles. In case A72-48, there are also four large bubbles and a small bubble, and similarly, four large bubbles are distributed symmetrically on both sides of the small bubble ($t = 1041\mu$s). However, spikes between the two large bubbles are more prominent than those between the large and small bubbles, which is contrary to case A72-24. Actually, the flow features in case A72-48 are quite similar to those in case I72-48. For these anti-phase cases, spikes between the large and small bubbles also skew

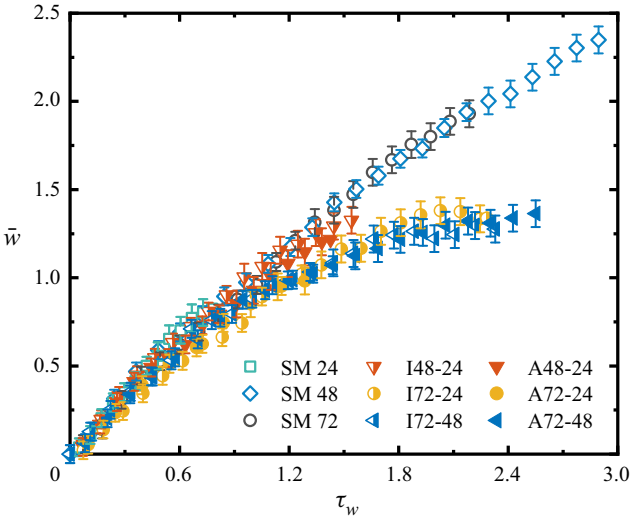

Figure 4. Comparison of dimensionless mixing width for single- and dual-mode cases.

towards the large bubble, whereas spikes between the two large bubbles develop without an inclination. Comparison with the in-phase cases indicates that the flow features also depend heavily on the initial phase difference.

3.2. *Mixing width and mode amplitude growths*

Variation of the dimensionless perturbation width (w) of each dual-mode case is given in figure 4. The time is scaled as $\tau_w = (m/R_0)v_w^{lin}(t - t^*)$, where v_w^{lin} is the experimental linear growth rate of the width and t^* the time when compression phase ends. The width is normalized as $\bar{w} = (m/R_0)(w - w^*)$, where w^* is the perturbation width at $t = t^*$. The perturbation widths of single-mode cases are also provided for comparison to evaluate the mode-coupling effects. Generally, the perturbation width of each dual-mode case develops similarly to its single-mode counterpart at early times, but grows slower from the middle to late stages. This indicates that mode coupling occurs from the middle stage and suppresses the perturbation width development. A similar conclusion was also drawn by Miles *et al.* (2004). Liang *et al.* (2021*a*) reported in their planar multi-mode RM instability study that although the mode-coupling effects reduce global mixing, they enhance local mixing. The perturbation width seems to be affected less significantly by initial phase difference. Miles *et al.* (2004) also concluded that the phase-difference effect is limited during the linear and early nonlinear stages, but becomes prominent during the deep nonlinear stage.

Distinct interfacial morphologies facilitate the recognition of interface contours, and a spectrum analysis can therefore be performed. By using an image processing program (Guo *et al.* 2022; Liang & Luo 2022), the interface profile is first extracted. Taking case I72-48 as an example, as shown in figure 5, the white dotted lines overlayed on two schlieren images at different moments are the interface profiles extracted for Fourier analysis. Although the very small vortex structures on the spikes are not identified, the main features of the interface are well captured. Then, by applying the fast Fourier transform, amplitude developments of the fundamental modes are obtained, as shown in figure 6. The dimensionless time is $\tau = (24/R_0)v^{lin}(t - t^*)$, with v^{lin} being the experimental linear growth rate of the mode amplitude. The amplitude is scaled as

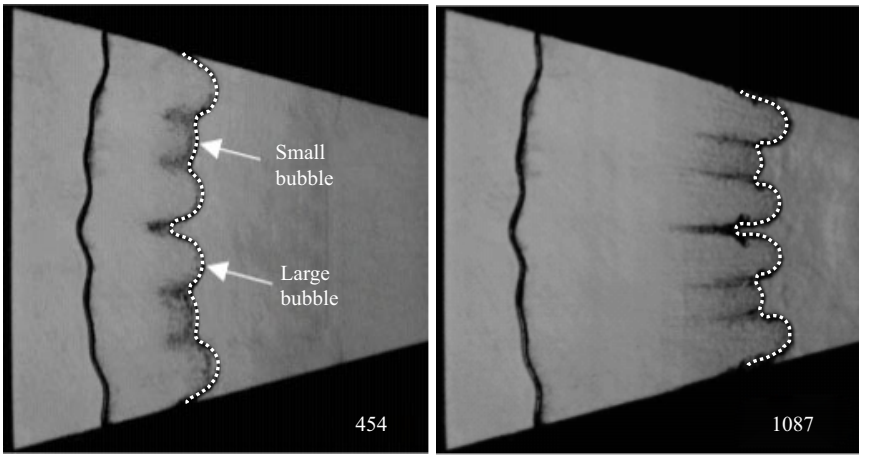

Figure 5. Comparison of the interface profile extracted with the actual interface at two different moments for case I72-48.

$\alpha = (24/R_0)(a - a^*)$, where a^* is the mode amplitude at $t = t^*$. Although Fourier analysis becomes strictly invalid once the vortex rolls up, the interfaces are still analysed through fast Fourier transform before the vortex is further developed to obtain more information of the fundamental mode amplitude. This treatment may lead to probable misidentification of extremely high-order mode amplitudes, but has a limited effect on the fundamental low-order mode amplitude. To explore the mode-coupling effects in dual-mode interface evolution, the first-order mode amplitudes in the corresponding single-mode cases are also provided.

As shown in figure 6(*a*), the amplitude of the mode with mode number 24 (*m*24 mode for short) in case I48-24 is much smaller than that in the single-mode case, i.e. the *m*24 mode amplitude growth is suppressed by mode coupling. On the contrary, the *m*24 mode amplitude in case A48-24 is slightly larger than that in the single-mode case, i.e. the *m*24 mode amplitude growth is promoted by mode coupling. This implies that the role of mode coupling is affected by the phase difference of the two fundamental modes. Comparing case I48-24 with case I72-24, the *m*24 mode amplitude growth is suppressed in the former but is promoted in the latter, which indicates that the role of mode coupling is also affected by the mode number combination. In ICF, the lower-*m* mode amplitude growth is generally severe and takes a long time to saturate, which will result in severe deformation of the hotspot interface and sharp decrease of the hotspot volume (Dittrich *et al.* 2014). Through designing the initial perturbation spectrum, one may expect to suppress the amplitude growth of the lower-*m* mode. In figure 6(*b*), the *m*48 mode amplitude growth in case A72-48 is almost consistent with that in the single-mode case during the time studied, which indicates that the mode-coupling effects on this mode evolution are negligible. Similar phenomena are found in the amplitude growths of the *m*48 mode in case I72-48 (although it shows a slight suppression after $\tau \sim 0.25$) and the *m*72 mode in case A72-24, as given in figure 6(*c*). In short, the mode-coupling effects in convergent geometry are still strongly dependent upon the initial perturbation spectrum.

To predict the amplitude signs of the modes generated in convergent geometry, based on the second-order solution derived by Haan (1991) in planar geometry, Zhou *et al.* (2020) proposed a modified model, named the modified Haan model, which is given as

$$a_{k_j \pm k_i} \approx \pm \tfrac{1}{2}(k_j \pm k_i) a^L_{k_i} a^L_{k_j}, \tag{3.1}$$

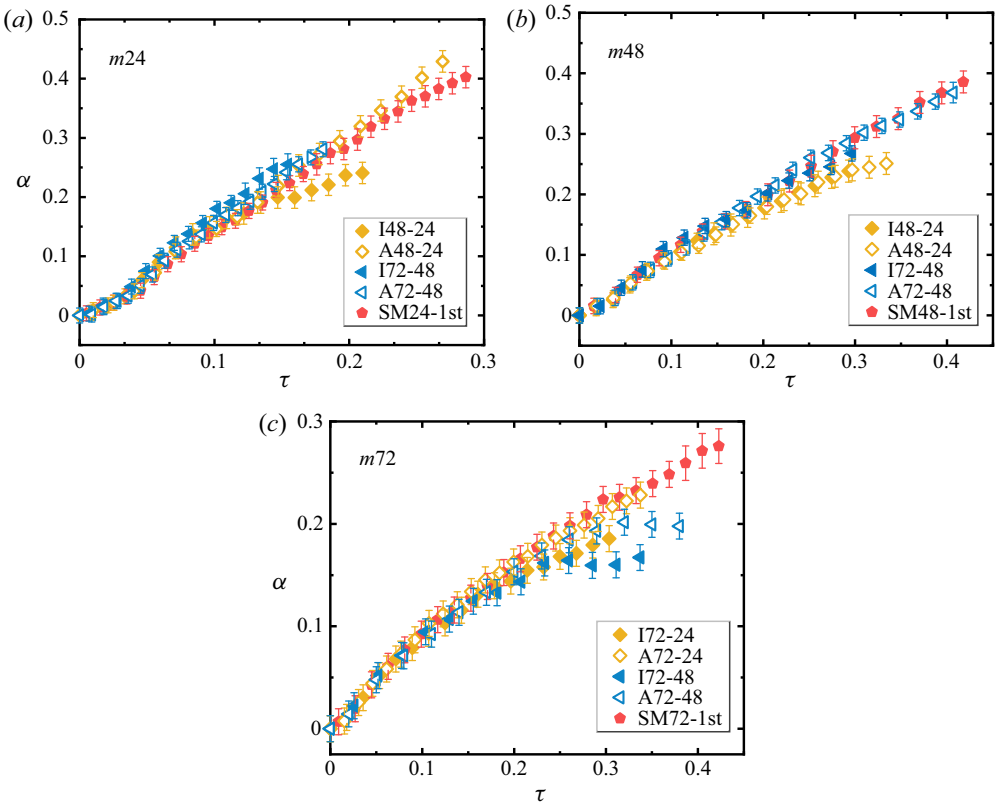

Figure 6. Comparison of dimensionless amplitudes of the fundamental modes for all dual-mode cases. The first-order mode amplitudes in corresponding single-mode cases are also provided.

where k is the wavenumber and a_k^L is the mode-k amplitude. From the amplitude signs of the modes generated, as provided in table 4, the mode-coupling effects on the amplitude growths of the fundamental modes can be demonstrated. For example, in case I48-24, the harmonic with mode number of 24 generated by coupling between fundamental modes has a negative amplitude, suppressing the $m24$ amplitude growth. In planar geometry (Luo *et al.* 2020), the authors found that for the initial dual-mode interface with combination of k and $k/3$ modes, mode coupling has a negligible influence on the growth of each basic wave. In convergent geometry, however, the $m72$ amplitude growth in case I72-24 is greatly suppressed, and the $m24$ amplitude growth is slightly promoted, as shown in figure 6. In case I72-24, coupling between positive $m72$ and positive $m24$ will generate the harmonics of positive $m96$ and negative $m48$. Further, coupling between negative $m48$ and positive $m24$ will generate negative $m72$ and positive $m24$, and coupling between positive $m96$ and positive $m24$ will also generate negative $m72$. As a result, the $m72$ amplitude growth is greatly suppressed, whereas the $m24$ amplitude growth is slightly promoted. For clarity, the amplitude signs of fundamental modes resulting from the feedback of second-order harmonics are listed in table 5. In other words, the feedback of second-order harmonics to fundamental modes becomes prominent in convergent geometry. Because the experimental time in this work is similar to that in previous work (Luo *et al.* 2020), we can conclude that the BP effect promotes the occurrence of mode coupling, and the feedback

a_{m_1}	a_{m_2}	$a_{m_1+m_2}$	$a_{m_1-m_2}$
+	+	+	−
−	+	−	+
+	−	−	+
−	−	+	−

Table 4. Amplitude signs of the modes generated by mode coupling.

Case	Basic modes	[+72, +24]	[+72, +48]			growth
I48-24	+48	−				↓
	+24		−			↓
		[+96, +24]	[+72, −48]	[+96, +72]	(−48, +24)	growth
I72-24	+72	−			−	↓
	+24		+	−	+	unsure
		[+72, +120]	[+72, −24]	[+48, +120]	(+48, −24)	growth
I72-48	+72			−	−	↓
	+48	−	+			unsure
		[−72, +24]	[−72, −48]			growth
A48-24	−48	+				↓
	+24		−			↓
		[−96, +24]	[−72, +48]	[−96, −72]	(+48, +24)	growth
A72-24	−72	+			+	↓
	+24		+	−	−	unsure
		[−72, −120]	[−72, +24]	[−120, +48]	(+48, +24)	growth
A72-48	−72			+	+	↓
	+48	+	−			unsure

Table 5. Amplitude signs of fundamental modes resulting from the feedback of second-order harmonics. The $[i, j]$ indicates mode coupling between the i mode and j mode before there is a saturated mode, because a saturated mode k has no contribution to the generation of lower-k mode, and can be affected only by coupling of two lower-k modes (Ofer *et al.* 1996). The (i, j) indicates mode coupling between the i mode and j mode during the whole time studied. The arrow ↓ means that the amplitude growth is inhibited.

of high-order modes to fundamental mode also arises earlier in convergent geometry than that in its planar counterpart.

Note that the $m72$ mode amplitude growth in the I/A72-48 cases almost stagnates at the late stage, but such a phenomenon has not been observed in the I/A72-24 cases. From the perspective of energy transfer, due to the presence of the $m48$ mode which acts as a transitional role between the $m24$ and $m72$ modes, energy is more easily transferred from higher-m modes to lower-m modes. Therefore, the $m72$ mode amplitude growth in the I/A72-48 cases saturates much earlier than in the I/A72-24 cases. For multi-mode cases, a collective band saturation amplitude $S(k)$ was introduced by Haan (1989). The mode whose amplitude reaches $S(k)$ is considered to be saturated. Provided that the initial spectrum is a smooth one, i.e. all neighbouring mode amplitudes are roughly equal initially, they showed that local structures with much larger amplitude than that of the individual mode will be formed by neighbouring modes. The local structure encounters large kinematic drag, leading to a much lower saturation amplitude $S(k)$ than 0.1λ (λ is the mode wavelength) for the individual mode (Shvarts *et al.* 1995; Ofer *et al.* 1996).

This means that the constituent modes in multi-mode cases with such an initial spectrum are more likely to enter the nonlinear stage due to mode coupling. However, Ofer *et al.* (1996) pointed out that for the initial dual-mode spectrum, $S(k)$ of the mode should still be taken as 0.1λ until there are saturated modes at the late stage. After that, the mode-coupling effects gradually become prominent, and the low-order and high-order harmonics are continuously generated and accumulated, which enables the concept of collective band saturation amplitude to take effect again.

The influence of mode coupling on saturation time (the time when a given mode amplitude grows to 0.1λ) of main modes is shown in figure 7. In all dual-mode cases, the higher-m fundamental mode amplitude always reaches saturation first. The two fundamental modes' amplitudes in the I/A72-48 cases are both saturated within the experimental time, whereas only the higher-m fundamental mode amplitude saturates in the other cases. The dimensionless saturation times when the modes just reach their saturation amplitudes are also marked in figure 7. To highlight the mode-coupling effects, the same method is used to obtain the dimensionless saturation time of the fundamental mode in the single-mode cases. Comparison of dimensionless saturation times for different cases is provided in table 6. Note that the fundamental mode $m72$ amplitude saturates at $\tau \sim 0.18$, but before this time the mode-coupling effects on its growth are less significant, as shown in figure 6. As a result, the evolution before saturation is almost the same as that in the single-mode case, resulting in the same saturation time. Similarly, the saturation times of mode $m48$ in the I/A72-48 cases are consistent with the single-mode results. However, for mode $m48$ in the I/A48-24 cases, amplitude saturation is not achieved by the time that mode coupling occurs ($\tau \sim 0.15$). Because mode coupling suppresses the $m48$ mode amplitude growth, its saturation time is therefore delayed relative to the single-mode case. In short, the fundamental mode combination affects the saturation time, but the initial phase difference has a limited effect on the saturation time.

To determine the dominant modes in dual-mode cases, the evolution of the average mode number is studied. The definition of the average mode number is given as

$$\langle m \rangle = \sum_m (a_m^2 \times m) \Big/ \sum_m a_m^2, \tag{3.2}$$

where m refers to all main modes on the spectrum and a_m represents the amplitude of mode m. Generally, the average mode number development can be divided into three stages marked with different colour blocks in figure 8. At stage I, the average mode number decreases, because the fundamental mode amplitude reduces due to shock compression. At stage II, the average mode number increases because of incipient development of the fundamental modes after shock impact. At stage III, the average mode number gradually reduces as time proceeds in all cases except I48-24. The reduction of the average mode number indicates that energy in the spectrum is generally transferred from higher-m modes to lower-m modes, and finally the lower-m modes dominate the spectrum. This is well known as the inverse cascade process, corresponding to the bubble merger process. Shvarts *et al.* (1995) numerically discussed the variation of the average wavenumber in 3-D planar multi-mode RT instability, and found that the spectrum becomes increasingly peaked towards lower k and the mean wavenumbers decrease in time as in the two-dimensional (2-D) case. That is, the 3-D case is shown to share many qualitative features with the 2-D case, such as an inverse cascade of large structure generation. The inverse cascade process is believed to be a common feature of multi-mode flows in both 3-D and 2-D flows. This work gives the quantitative description of the inverse cascade

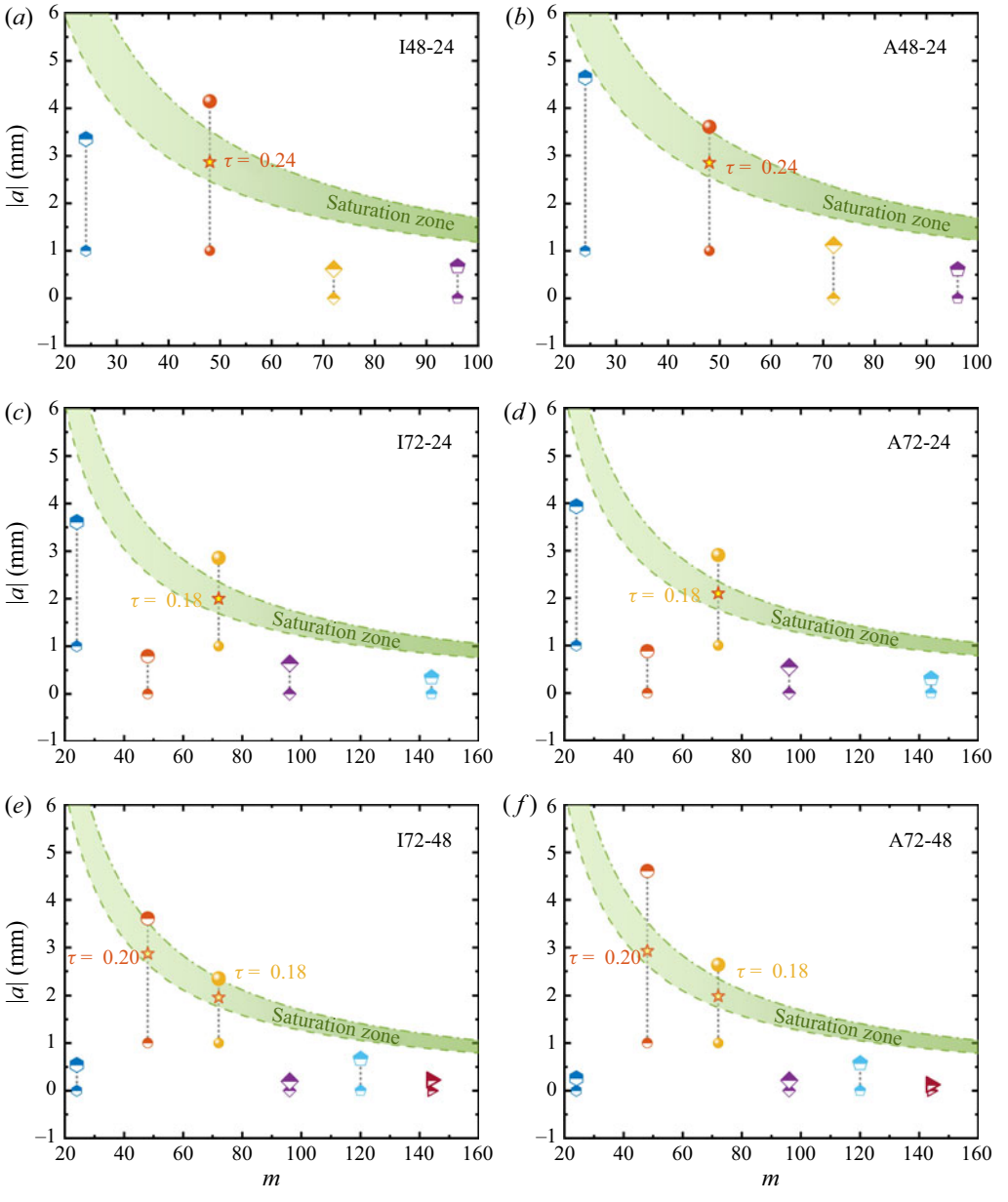

Figure 7. The absolute values of main modes' amplitudes comparing with their 0.1λ in all cases. The 'saturation zone' means that the mode reaches its saturated amplitude (0.1λ), and the borders are determined by variation of the saturated mode amplitude (0.1λ) with the mode number at initial and final moments during the time studied. Different symbols represent different modes. For each mode, two amplitudes at initial and final moments are provided. The dimensionless times marked correspond to the times when the modes have just reached their saturation amplitudes.

process from the perspective of the average mode number in the 2-D dual-mode RM instability. In case I48-24, the bubble merger process is absent as shown in figure 2. Thus its average mode number does not decrease, and the higher-m fundamental mode is dominant. This conclusion is consistent with the observation in figure 7. In short, the

Case	SM-1st	I48-24	A48-24	I72-24	A72-24	I72-48	A72-48
Mode number 24	0.26	—	—	—	—	—	—
Mode number 48	0.20	0.24	0.24	—	—	0.20	0.20
Mode number 72	0.17	—	—	0.18	0.18	0.18	0.18

Table 6. The dimensionless saturation times of modes in single- and dual-mode cases. The dashes mean that the corresponding fundamental mode does not saturate or exist in this case.

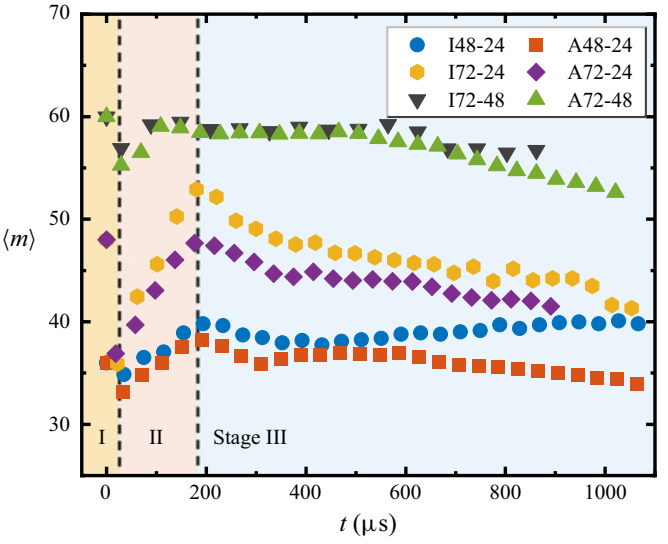

Figure 8. Development of average mode number of spectrum in all cases. The colour blocks represent three different stages.

average mode number reduction at stage III is ascribed to amplitude saturation of higher-m modes and generation of lower-m modes due to mode coupling.

3.3. *Theoretical prediction of the mode amplitude*

3.3.1. *Theoretical models for planar geometry*

The RT effect and reshock are eliminated in the current convergent geometry, which provides a possibility to evaluate the BP effect on the fundamental mode development. In planar geometry, Ofer *et al.* (1996) solved the modal model proposed by Haan (1991), and obtained a second-order solution for multi-mode RT instability, which is written as

$$a_k(t) = a_k^{lin}(t) - \tfrac{1}{2}kA\left(\sum_{k'} a_{k'}^{lin}(t)a_{k+k'}^{lin}(t) - \tfrac{1}{2}\sum_{k'<k} a_{k'}^{lin}(t)a_{k-k'}^{lin}(t)\right), \tag{3.3}$$

where $k, k' \in \mathbb{R}^+$ and $a_k^{lin}(t)$ is the k mode amplitude at the linear stage. The second term on the right-hand side of (3.3) represents the contributions of mode $(k + k')$ and mode $(k - k')$ to k mode generation. To apply (3.3) to the RM instability, through replacing the constant acceleration g with an impulsive acceleration $\delta t \Delta v$, Luo *et al.* (2020) deduced a dual-mode modal model, named the RM-Ofer model. By applying the RM-Ofer model to

a dual-mode RM instability with fundamental k and $k/2$ modes, the growth rates of the fundamental modes and the harmonic generated can be given as

$$\left.\begin{aligned} v_{k/2}(t) &= v_{k/2}^{lin} - \tfrac{1}{2}kA^+\left[\left(\sqrt{2}+\tfrac{1}{2}\right)v_k^{lin}a_{k/2}^+ + v_k^{lin}v_{k/2}^{lin}t + \tfrac{1}{2}v_{k/2}^{lin}a_k^+\right], \\ v_k(t) &= v_k^{lin} + \tfrac{1}{2}kA^+(2v_{k/2}^{lin}a_{k/2}^+ + v_{k/2}^{lin}v_{k/2}^{lin}t), \\ v_{3k/2}(t) &= \tfrac{3}{8}kA^+[2v_{k/2}^{lin}v_k^{lin}t + v_{k/2}^{lin}a_k^+ + (1+\sqrt{2})v_k^{lin}a_{k/2}^+], \end{aligned}\right\} \tag{3.4}$$

where a_k^+ is the postshock amplitude of mode k. The RM-Ofer model considers mode coupling, but ignores nonlinearity. Therefore, it fails to predict the mode amplitude growth when nonlinearity is prominent (Luo *et al.* 2020). To evaluate nonlinearity, a planar dual-mode model combining the nonlinear single-mode model proposed by Zhang & Guo (2016) with the RM-Ofer model, named the mZG-Ofer model, has been proposed by Luo *et al.* (2020). The mZG-Ofer model is expressed as

$$\left.\begin{aligned} v_{k/2}(t) &= \frac{v_{k/2}^{lin} - \tfrac{1}{2}kA^+\left[\left(\sqrt{2}+\tfrac{1}{2}\right)v_k^{lin}a_{k/2}^+ + v_k^{lin}v_{k/2}^{lin}t + \tfrac{1}{2}v_{k/2}^{lin}a_k^+\right]}{1+\hat{a}k\left\{v_{k/2}^{lin} - \tfrac{1}{2}kA^+\left[\left(\sqrt{2}+\tfrac{1}{2}\right)v_k^{lin}a_{k/2}^+ + v_k^{lin}v_{k/2}^{lin}t + \tfrac{1}{2}v_{k/2}^{lin}a_k^+\right]\right\}t}, \\ v_k(t) &= \frac{v_k^{lin} + \tfrac{1}{2}kA^+(2v_{k/2}^{lin}a_{k/2}^+ + v_{k/2}^{lin}v_{k/2}^{lin}t)}{1+\hat{a}k[v_k^{lin} + \tfrac{1}{2}kA^+(2v_{k/2}^{lin}a_{k/2}^+ + v_{k/2}^{lin}v_{k/2}^{lin}t)]t}, \\ v_{3k/2}(t) &= \frac{\tfrac{3}{8}kA^+[2v_{k/2}^{lin}v_k^{lin}t + v_{k/2}^{lin}a_k^+ + (1+\sqrt{2})v_k^{lin}a_{k/2}^+]}{1+\tfrac{3}{8}\hat{a}k^2A^+[2v_{k/2}^{lin}v_k^{lin}t + v_{k/2}^{lin}a_k^+ + (1+\sqrt{2})v_k^{lin}a_{k/2}^+]\}t}, \\ \hat{a} &= \tfrac{3}{4}\frac{(1-A^+)(3-A^+)}{3-A^+ + \sqrt{2}(1-A^+)^{1/2}}\frac{4(3-A^+) + \sqrt{2}(9-A^+)(1-A^+)^{1/2}}{(3-A^+)^2 + 2\sqrt{2}(3+A^+)(1-A^+)^{1/2}}. \end{aligned}\right\} \tag{3.5}$$

The mZG-Ofer model considers both mode coupling and nonlinearity, and its applicability in predicting the mode amplitude nonlinear growth of dual-mode interfaces subjected to planar shock waves has been verified (Luo *et al.* 2020).

Comparison of the experimental results with theoretical predictions from the mZG-Ofer model is given in figure 9. The model gives a good prediction for the higher-m fundamental mode amplitude growth, but it greatly underestimates the lower-m fundamental mode amplitude growth. This indicates that the BP effect cannot be ignored, and it has a stronger effect on the lower-m mode growth than the higher-m mode. A similar conclusion was also drawn in previous theoretical work on single-mode perturbations (Wang *et al.* 2015), and our work provides additional experimental evidence. In addition, the mZG-Ofer model generally provides good predictions for amplitude growth rates of the modes generated because they generally have high mode numbers. In experiments, the amplitude signs of $m_1 + m_2$ mode and $m_1 - m_2$ mode generated in in-phase (anti-phase) cases are positive (negative) and negative (positive), respectively, which are consistent with the theoretical predictions from the modified Haan model, as shown in table 4. As a result, the amplitude signs of the modes generated by mode coupling in convergent geometry can also be predicted by Haan's solution proposed for planar geometry.

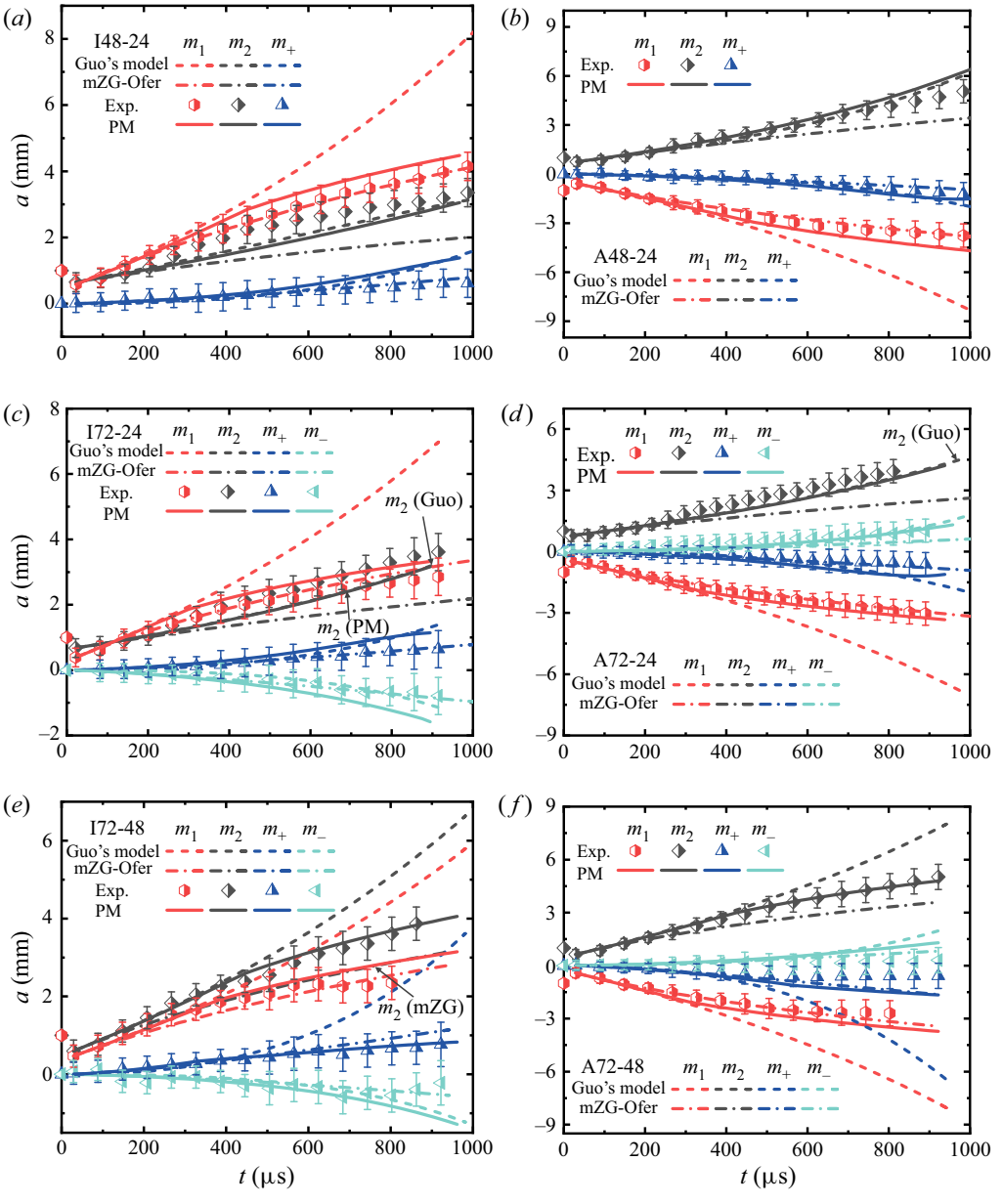

Figure 9. Variations of amplitudes of fundamental modes and modes generated with time. Theoretical results from the mZG-Ofer model, Guo's model and PM model are shown to compare with experimental results. Here m_+ and m_- refer to $m_1 + m_2$ mode and $m_1 - m_2$ mode.

3.3.2. *Theoretical models for convergent geometry*

In convergent geometry, according to previous work (Bell 1951; Mikaelian 2005*a*), the linear solution of a single-mode growth rate in a pure BP environment can be expressed as

$$\dot{a}(t) = v_0 C_r^2, \tag{3.6}$$

where $v_0 = a_0^+ \Delta v(mA - 1)/R_0$ is the initial growth rate and $C_r = R_0/R$ is the convergence ratio with $R = R_0 + Vt$ (V is the constant interface velocity). To quantify

nonlinearity in the single-mode interface evolution, the expression for third-order feedback to the fundamental mode was obtained by Wang *et al.* (2015), which is given as

$$\begin{aligned} a_f = {} & a_0^3\frac{1}{8}\left(3\frac{m^2}{R^2}-\frac{A}{R}\frac{m}{R}\right)\left(1-\frac{1}{C_r}\right)^2 + a_0^2 v_0 \frac{1}{24}t\left[(7-8A^2)\frac{m^2}{R^2}-\frac{19Am-18}{R^2}\right]C_r \\ & + a_0^2 v_0 \frac{1}{24}t\left\{2\left[(8A^2-10)\frac{m^2}{R^2}+7\frac{A}{R}\frac{m}{R}-\frac{3}{R^2}\right]-\left[(8A^2-13)\frac{m^2}{R^2}-5\frac{A}{R}\frac{m}{R}+\frac{12}{R^2}\right]\frac{1}{C_r}\right\} \\ & + a_0 v_0^2 \frac{1}{24}t^2\left\{\left[(A^2+2)\frac{m^2}{R^2}-22\frac{A}{R}\frac{m}{R}+\frac{27}{R^2}\right]C_r^2+2\left[(5A^2-5)\frac{m^2}{R^2}+13\frac{A}{R}\frac{m}{R}-\frac{3}{R^2}\right]C_r\right\} \\ & - a_0 v_0^2 \frac{1}{24}t^2\left[(11A^2-5)\frac{m^2}{R^2}-2\frac{A}{R}\frac{m}{R}\right] + v_0^3 t^3\left(\frac{1}{120}A^2\frac{m^2}{R^2}-\frac{11}{60}A\frac{1}{R}\frac{m}{R}+\frac{3}{8}\frac{1}{R^2}\right)C_r^3 \\ & - v_0^3 t^3\left\{\left[\left(\frac{1}{60}A^2+\frac{1}{12}\right)\frac{m^2}{R^2}-\frac{11}{30}\frac{A}{R}\frac{m}{R}\right]C_r^2+\left[\left(\frac{19}{120}A^2-\frac{1}{24}\right)\frac{m^2}{R^2}+\frac{1}{60}\frac{A}{R}\frac{m}{R}\right]C_r\right\}. \end{aligned} \tag{3.7}$$

The nonlinear effects on the single-mode perturbation growth in a pure BP environment were found to be reasonably evaluated by (3.7) (Luo *et al.* 2019). Recently, by solving the governing equations for multi-mode perturbation growth on a cylindrically convergent interface, Guo *et al.* (2020) obtained second-order weakly nonlinear solutions for dual-mode perturbations in a pure BP environment, which are expressed as

$$\left.\begin{aligned} a_{1,m_1} &= a_{m_1}^0 + \dot{a}_{m_1}^0 C_r t, \\ a_{1,m_2} &= a_{m_2}^0 + \dot{a}_{m_2}^0 C_r t, \\ a_+ &= (a_{m_2}^0 \dot{a}_{m_1}^0 + a_{m_1}^0 \dot{a}_{m_2}^0)\frac{1}{2R}[A(m_1+m_2)-1](C_r-1)t \\ &\quad + \dot{a}_{m_1}^0 \dot{a}_{m_2}^0 \frac{1}{6R}[A(m_1+m_2)(C_r^2-4C_r)-3C_r^2]t^2, \\ a_- &= \frac{1}{2R}[A(m_1-m_2)(a_{m_1}^0 \dot{a}_{m_2}^0 - a_{m_2}^0 \dot{a}_{m_1}^0) \\ &\quad - (a_{m_1}^0 \dot{a}_{m_2}^0 + a_{m_2}^0 \dot{a}_{m_1}^0)](C_r-1)t \\ &\quad + \dot{a}_{m_1}^0 \dot{a}_{m_2}^0 \frac{1}{6R}[A(m_1-m_2)(C_r^2+2C_r)-3C_r^2]t^2, \end{aligned}\right\} \tag{3.8}$$

where $a_{1,m}$ refers to the linear solutions for the dual-mode BP growth, a_m^0 is the initial perturbation amplitude of the m mode and $\dot{a}_m^0$ is the initial growth rate. The subscripts $+$ and $-$ represent the modes m_1+m_2 and m_1-m_2, respectively. This model is named Guo's model hereafter. Since the model solves the second-order governing equations, it only gives a linear solution to the growth of the fundamental mode, and does not consider mode coupling. However, for the modes m_1+m_2 and m_1-m_2, the solution does consider both the BP effect and mode coupling.

The predictions from Guo's model are illustrated in figure 9. For the mode generated, the model only provides good predictions to the amplitude growth at the early stage, because the amplitude growth has entered the strongly nonlinear stage at late times. For the fundamental mode, the model behaves differently. In the I/A48-24 and I/A72-24 cases, the model generally predicts well the lower-m mode amplitude growth, but it greatly

overestimates the higher-m mode amplitude growth at the early stage. This implies that the higher-m (lower-m) fundamental mode amplitude growth is more significantly affected by mode coupling (BP effect). In the I/A72-48 cases, however, both higher- and lower-m modes are overestimated by the model, probably because nonlinearity that gradually becomes significant after mode saturation has not been considered in the model. From the discussion on the mode saturation time, the higher-m mode amplitude reaches saturation earlier, and the amplitudes of both fundamental modes saturate in the I/A72-48 cases. In short, for the fundamental mode which reaches (does not reach) its saturation amplitude, its amplitude growth cannot (can) be predicted by Guo's model.

3.3.3. *The present model*

To reasonably evaluate the amplitude growths of the fundamental modes and modes generated, the BP effect and mode coupling as well as nonlinearity should be considered in the model. In this work, the amplitude of mode m is considered to be composed of two parts, i.e.

$$a_m = a_m^{lin} + a_m^{nonlin}, \tag{3.9}$$

where a_m^{lin} is the linear amplitude and a_m^{nonlin} is the nonlinear feedback from the third-order harmonic to mode m. Amplitude a_m^{lin} is calculated by

$$a_m^{lin} = \int_{t_0^+}^{t} v_{mc} C_r^2 \, \mathrm{d}t, \tag{3.10}$$

where v_{mc} is the growth rate given by (3.4), t_0^+ is the time just after the shock passage and a_m^{nonlin} is obtained through substituting v_0 and a_0 by v_{mc} and a_{mc} respectively in (3.7). Note that the wavenumber k is calculated as m/R in convergent RM instability. For lower-m modes, nonlinearity is negligible, and, thus, only the first term in (3.9) is retained. Note that (3.9) can degenerate to a_{mc} calculated by (3.4) when the BP effect and nonlinearity are absent, i.e. $C_r = 1$, in which case the limit of large R as $m/R \to k$ is adopted and the second term in (3.9) is equal to zero. It can also reduce to (3.6) when both mode coupling and nonlinearity are not considered, i.e. $v_m^{lin} a_m^+$ and $v_m^{lin} v_m^{lin}$ in (3.4) and the second term in (3.9) is equal to zero. In addition, when $m \to 0$, the items related to mode coupling in (3.9) tend to zero, and (3.9) will degenerate to (3.6). This verifies the conclusion that lower-m mode amplitude growth is more heavily affected by the BP effect. After the mode amplitude reaches saturation, nonlinearity is significant, but (3.7), from which a_m^{nonlin} is obtained, is only valid for weakly nonlinear stages (Wang *et al.* 2015). For multi-mode initial spectra, Ofer *et al.* (1996) considered that the mode amplitude growth obeys the following relation after saturation:

$$a_m^{sat}(t) = a_m^{t_{sat}} \left[1 + \log \left(\frac{a_m^{lin}(t)}{a_m^{lin}(t_{sat})} \right) \right], \tag{3.11}$$

where $a_m^{sat}(t)$ is the amplitude of mode m after saturation, $a_m^{t_{sat}}$ is the saturation amplitude (here given by 0.1λ) and t_{sat} is the time at which saturation occurs. This post-saturation relation has been verified in convergent geometry (Milovich *et al.* 2004; El Rafei *et al.* 2019). In this work, the post-saturation relation is adopted in the model to evaluate the saturated mode's nonlinear behaviour. To sum up, (3.9)–(3.11) constitute the present model (named the PM model).

The PM model indicates that the mode amplitude develops as a $1/t$ decay after saturation, which is consistent with the late bubble growth rate of multi-mode RM instability given by both potential flow models (Alon *et al.* 1994, 1995; Oron *et al.* 2001) and vortex models (Rikanati, Alon & Shvarts 1998). The results in figure 9 show that the PM model generally gives good predictions for the amplitude growths of the fundamental modes with both lower and higher mode numbers. Relatively, the PM model provides a better prediction for the amplitude growth of the fundamental mode with a higher (lower) mode number than Guo's (mZG-Ofer) model. For the fundamental mode with a higher mode number, the PM model slightly overestimates the experimental result. First, the fundamental mode with a higher mode number is less affected by the BP effect which always promotes the perturbation growth. Second, the RM-Ofer model is only accurate to second-order precision and does not consider the feedback from the high-order harmonics. However, the feedback from the second-order harmonics always inhibits the development of the fundamental mode with a higher mode number, as indicated in table 5. For the fundamental mode with a lower mode number, the feedback behaves differently, and it is difficult to determine its role. In addition, the PM model greatly improves the predictions for the amplitude growths of the saturated modes relative to Guo's model. For the modes generated, the PM model provides good predictions at the early stage, but slightly overestimates at the late stage, probably because the BP effect is involved in the model.

In summary, for the development of the fundamental mode which does not reach its saturation amplitude, its amplitude growth is more affected by the BP effect than mode coupling. For the development of the fundamental mode which reaches its saturation amplitude, its amplitude growths are more significantly affected by mode coupling than the BP effect. After the mode reaches its saturation amplitude, the amplitude growth can be described by the post-saturation relation given by Ofer *et al.* (1996).

4. Conclusion

Shock-tube experiments on the development of a dual-mode air–SF_6 interface subjected to a convergent shock wave are carried out. The convergent shock tube is specially designed with a tail opening to eliminate the RT effect and reshock, and to highlight the BP effect on mode amplitude growth. Six kinds of dual-mode interface with different initial perturbation spectra that are produced by changing the mode combination and phase difference between fundamental modes are considered. The results show that the flow features are strongly dependent upon the initial spectrum. At the late stage, the flow is generally dominated by bubbles with different sizes. The number and arrangement of large bubbles and small bubbles as well as the inclination of spikes are closely associated with the mode combination and phase difference.

The developments of perturbation mixing width show that for dual-mode case, mode coupling arises from the middle stage and suppresses the width growth compared with the single-mode counterpart. Depending upon the initial spectrum, the fundamental mode amplitude growth is either promoted, inhibited or unaffected by mode coupling. In general, mode coupling inhibits the amplitude growth of the fundamental mode with a higher mode number, but causes different behaviours for the amplitude growth of the fundamental mode with a lower mode number. The fundamental mode amplitude variation can be explained by the feedback of the high-order modes. The BP effect promotes the occurrence of mode coupling, and the feedback of high-order modes to fundamental mode also arises earlier in convergent geometry than that in its planar counterpart. Moreover, the amplitude growth

is found to saturate earlier for the fundamental mode with a higher mode number, and the saturation time is affected by mode coupling. By introducing the concept of the average mode number, the flow is found to be dominated by the fundamental mode with a lower mode number.

By incorporating mode coupling and nonlinearity into the planar dual-mode model, a model is established to predict the amplitude growth of the fundamental mode. The model provides good (poor) predictions for the amplitude growth of the fundamental mode with a higher (lower) mode number, which indicates that the amplitude growth of the fundamental mode with a lower mode number is more significantly affected by the BP effect which is not included in the model. Further, an existing convergent dual-mode model (Guo *et al.* 2020) considering the BP effect and weak nonlinearity is used to predict the amplitude growths of the fundamental modes and modes generated. For the modes generated, the model can predict the amplitude growths at the early stage. For the fundamental mode with a lower mode number that does not reach its saturation amplitude, the model provides a good prediction, whereas for the fundamental mode with a higher mode number that reaches its saturation amplitude, the prediction is less satisfactory. This indicates that the fundamental mode with a higher (lower) mode number is more heavily affected by mode coupling (BP effect). Finally, the amplitude developments of the fundamental modes and modes generated can be reasonably well predicted by combining the planar mode-coupling model, the linear BP model and the third-order feedback model. In particular, for the fundamental mode that reaches its saturation amplitude, the post-saturation relation given by Ofer *et al.* (1996) is introduced into the model to achieve a better prediction.

This work can provide a support for designing the initial mode combination when one wants to manipulate the mode amplitude growth. In future work, development of multi-mode perturbations subjected to a convergent shock wave will be investigated and a more complicated mode-coupling mechanism will be explored.

Funding. This work was supported by the National Natural Science Foundation of China (nos. 12022201, 91952205 and 12102425) and Youth Innovation Promotion Association CAS.

Declaration of interests. The authors report no conflict of interest.

Author ORCIDs.
Zhigang Zhai https://orcid.org/0000-0002-0094-5210;
Xisheng Luo https://orcid.org/0000-0002-4303-8290.

References

Alon, U., Hecht, J., Mukamel, D. & Shvarts, D. 1994 Scale invariant mixing rates of hydrodynamically unstable interface. *Phys. Rev. Lett.* **72**, 2867–2870.

Alon, U., Hecht, J., Ofer, D. & Shvarts, D. 1995 Power laws and similarity of Rayleigh–Taylor and Richtmyer–Meshkov mixing fronts. *Phys. Rev. Lett.* **74**, 534–537.

Balakumar, B.J., Orlicz, G.C., Ristorcelli, J.R., Balasubramanian, S., Prestridge, K.P. & Tomkins, C.D. 2012 Turbulent mixing in a Richtmyer–Meshkov fluid layer after reshock: velocity and density statistics. *J. Fluid Mech.* **696**, 67–93.

Bell, G.I. 1951 Taylor instability on cylinders and spheres in the small amplitude approximation. *Tech. Rep.* LA-1321, LANL 1321.

Chu, Y., Wang, Z., Qi, J., Xu, Z. & Li, Z. 2022 Numerical performance assessment of double-shell targets for Z-pinch dynamic hohlraum. *Matt. Radiat. Extrem.* **7**, 035902.

Cohen, R.D. 1991 Shattering of a liquid drop due to impact. *Proc. R. Soc. Lond.* A **435**, 483–503.

Craxton, R., Anderson, K., Boehly, T., Goncharov, V., Harding, D., Knauer, J., McCrory, R., McKenty, P., Meyerhofer, D. & Myatt, J. 2015 Direct-drive inertial confinement fusion: a review. *Phys. Plasmas* **22**, 110501.

DI STEFANO, C., MALAMUD, G., KURANZ, C., KLEIN, S. & DRAKE, R. 2015*a* Measurement of Richtmyer–Meshkov mode coupling under steady shock conditions and at high energy density. *High Energ. Dens. Phys.* **17**, 263–269.

DI STEFANO, C., MALAMUD, G., KURANZ, C., KLEIN, S., STOECKL, C. & DRAKE, R. 2015*b* Richtmyer–Meshkov evolution under steady shock conditions in the high-energy-density regime. *Appl. Phys. Lett.* **106**, 114103.

DIMOTAKIS, P.E. 2000 The mixing transition in turbulent flows. *J. Fluid Mech.* **409**, 69–98.

DING, J., SI, T., YANG, J., LU, X., ZHAI, Z. & LUO, X. 2017 Measurement of a Richtmyer–Meshkov instability at an air-SF_6 interface in a semiannular shock tube. *Phys. Rev. Lett.* **119**, 014501.

DITTRICH, T.R., *et al.* 2014 Design of a high-foot high-adiabat ICF capsule for the national ignition facility. *Phys. Rev. Lett.* **112**, 055002.

EL RAFEI, M., FLAIG, M., YOUNGS, D.L. & THORNBER, B. 2019 Three-dimensional simulations of turbulent mixing in spherical implosions. *Phys. Fluids* **31**, 114101.

ELBAZ, Y. & SHVARTS, D. 2018 Modal model mean field self-similar solutions to the asymptotic evolution of Rayleigh–Taylor and Richtmyer–Meshkov instabilities and its dependence on the initial conditions. *Phys. Plasmas* **25**, 062126.

FINCKE, J.R., LANIER, N.E., BATHA, S.H., HUECKSTAEDT, R.M., MAGELSSEN, G.R., ROTHMAN, S.D., PARKER, K.W. & HORSFIELD, C.J. 2005 Effect of convergence on growth of the Richtmyer–Meshkov instability. *Laser Part. Beams* **23**, 21–25.

GONCHAROV, V.N. 2002 Analytical model of nonlinear, single-mode, classical Rayleigh–Taylor instability at arbitrary Atwood numbers. *Phys. Rev. Lett.* **88**, 134502.

GUO, H., CHENG, T. & LI, Y. 2020 Weakly nonlinear multi-mode Bell–Plesset growth in cylindrical geometry. *Chin. Phys.* B **29**, 115202.

GUO, X., CONG, Z., SI, T. & LUO, X. 2022 Shock-tube studies of single- and quasi-single-mode perturbation growth in Richtmyer–Meshkov flows with reshock. *J. Fluid Mech.* **941**, A65.

GUO, X., ZHAI, Z., SI, T. & LUO, X. 2019 Bubble merger in initial Richtmyer–Meshkov instability on inverse-chevron interface. *Phys. Rev. Fluids* **4**, 092001.

HAAN, S. 1989 Onset of nonlinear saturation for Rayleigh–Taylor growth in the presence of a full spectrum of modes. *Phys. Rev.* A **39**, 5812–5825.

HAAN, S.W. 1991 Weakly nonlinear hydrodynamic instabilities in inertial fusion. *Phys. Fluids* B **3**, 2349–2355.

JACOBS, J.W. 1992 Shock-induced mixing of a light-gas cylinder. *J. Fluid Mech.* **234**, 629–649.

JACOBS, J.W., JENKINS, D.G., KLEIN, D.L. & BENJAMIN, R.F. 1995 Nonlinear growth of the shock-accelerated instability of a thin fluid layer. *J. Fluid Mech.* **295**, 23–42.

JACOBS, J.W., KLEIN, D.L., JENKINS, D.G. & BENJAMIN, R.F. 1993 Instability growth patterns of a shock-accelerated thin fluid layer. *Phys. Rev. Lett.* **70**, 583–586.

JACOBS, J.W. & KRIVETS, V.V. 2005 Experiments on the late-time development of single-mode Richtmyer–Meshkov instability. *Phys. Fluids* **17**, 034105.

JOURDAN, G. & HOUAS, L. 2005 High-amplitude single-mode perturbation evolution at the Richtmyer–Meshkov instability. *Phys. Rev. Lett.* **95**, 204502.

KUMAR, S., HORNUNG, H.G. & STURTEVANT, B. 2003 Growth of shocked gaseous interfaces in a conical geometry. *Phys. Fluids* **15**, 3194–3207.

LANIER, N.E., BARNES, C.W., BATHA, S.H., DAY, R.D., MAGELSSEN, G.R., SCOTT, J.M., DUNNE, A.M., PARKER, K.W. & ROTHMAN, S.D. 2003 Multimode seeded Richtmyer–Meshkov mixing in a convergent, compressible, miscible plasma system. *Phys. Plasmas* **10**, 1816–1821.

LEINOV, E., MALAMUD, G., ELBAZ, Y., LEVIN, L.A., BEN-DOR, G., SHVARTS, D. & SADOT, O. 2009 Experimental and numerical investigation of the Richtmyer–Meshkov instability under re-shock conditions. *J. Fluid Mech.* **626**, 449–475.

LI, M., DING, J., ZHAI, Z., SI, T., LIU, N., HUANG, S. & LUO, X. 2020 On divergent Richtmyer–Meshkov instability of a light/heavy interface. *J. Fluid Mech.* **901**, A38.

LIANG, Y., LIU, L., ZHAI, Z., DING, J., SI, T. & LUO, X. 2021*a* Richtmyer–Meshkov instability on two-dimensional multi-mode interfaces. *J. Fluid Mech.* **928**, A37.

LIANG, Y., LIU, L., ZHAI, Z., SI, T. & LUO, X. 2021*b* Universal perturbation growth of Richtmyer–Meshkov instability for minimum-surface featured interface induced by weak shock waves. *Phys. Fluids* **33**, 032110.

LIANG, Y. & LUO, X. 2022 On shock-induced light-fluid-layer evolution. *J. Fluid Mech.* **933**, A10.

LIANG, Y., ZHAI, Z., DING, J. & LUO, X. 2019 Richtmyer–Meshkov instability on a quasi-single mode interface. *J. Fluid Mech.* **872**, 729–751.

LINDL, J., LANDEN, O., EDWARDS, J., MOSES, E. & TEAM, N. 2014 Review of the national ignition campaign 2009-2012. *Phys. Plasmas* **21**, 020501.

LIU, W.H., HE, X.T. & YU, C.P. 2012 Cylindrical effects on Richtmyer–Meshkov instability for arbitrary Atwood numbers in weakly nonlinear regime. *Phys. Plasmas* **19**, 072108.

LIU, L., LIANG, Y., DING, J., LIU, N. & LUO, X. 2018 An elaborate experiment on the single-mode Richtmyer–Meshkov instability. *J. Fluid Mech.* **853**, R2.

LIU, W.H., YU, C.P., YE, W.H., WANG, L.F. & HE, X.T. 2014 Nonlinear theory of classical cylindrical Richtmyer–Meshkov instability for arbitrary Atwood numbers. *Phys. Plasmas* **21**, 062119.

LOMBARDINI, M., PULLIN, D.I. & MEIRON, D.I. 2014 Turbulent mixing driven by spherical implosions. Part 1. Flow description and mixing-layer growth. *J. Fluid Mech.* **748**, 85–112.

LUO, X., DONG, P., SI, T. & ZHAI, Z. 2016 The Richtmyer–Meshkov instability of a 'V' shaped air/SF_6 interface. *J. Fluid Mech.* **802**, 186–202.

LUO, X., LI, M., DING, J., ZHAI, Z. & SI, T. 2019 Nonlinear behaviour of convergent Richtmyer–Meshkov instability. *J. Fluid Mech.* **877**, 130–141.

LUO, X., LIU, L., LIANG, Y., DING, J. & WEN, C. 2020 Richtmyer–Meshkov instability on a dual-mode interface. *J. Fluid Mech.* **905**, A5.

LUO, X., WANG, X. & SI, T. 2013 The Richtmyer–Meshkov instability of a three-dimensional air/SF_6 interface with a minimum-surface feature. *J. Fluid Mech.* **722**, R2.

LUO, X., ZHANG, F., DING, J., SI, T., YANG, J., ZHAI, Z & WEN, C. 2018 Long-term effect of Rayleigh–Taylor stabilization on converging Richtmyer–Meshkov instability. *J. Fluid Mech.* **849**, 231–244.

MARIANI, C., VANDENBOOMGAERDE, M., JOURDAN, G., SOUFFLAND, D. & HOUAS, L. 2008 Investigation of the Richtmyer–Meshkov instability with stereolithographed interfaces. *Phys. Rev. Lett.* **100**, 254503.

MCFARLAND, J., REILLY, D., BLACK, W., GREENOUGH, J. & RANJAN, D. 2015 Modal interactions between a large-wavelength inclined interface and small-wavelength multimode perturbations in a Richtmyer–Meshkov instability. *Phys. Rev.* E **92**, 013023.

MESHKOV, E.E. 1969 Instability of the interface of two gases accelerated by a shock wave. *Fluid Dyn.* **4**, 101–104.

MEYER, K.A. & BLEWETT, P.J. 1972 Numerical investigation of the stability of a shock-accelerated interface between two fluids. *Phys. Fluids* **15**, 753–759.

MIKAELIAN, K.O. 2005*a* Rayleigh–Taylor and Richtmyer–Meshkov instabilities and mixing in stratified cylindrical shells. *Phys. Fluids* **17**, 094105.

MIKAELIAN, K.O. 2005*b* Richtmyer–Meshkov instability of arbitrary shapes. *Phys. Fluids* **17**, 034101.

MILES, A.R., EDWARDS, M.J., BLUE, B., HANSEN, J.F., ROBEY, H.F., DRAKE, R.P., KURANZ, C. & LEIBRANDT, D.R. 2004 The effects of a short-wavelength mode on the evolution of a long-wavelength perturbatoin driven by a strong blast wave. *Phys. Plasmas* **11**, 5507–5519.

MILOVICH, J.L., AMENDT, P., MARINAK, M. & ROBEY, H. 2004 Multimode short-wavelength perturbation growth studies for the national ignition facility double-shell ignition target designs. *Phys. Plasmas.* **11**, 1552–1568.

MOHAGHAR, M., CARTER, J., MUSCI, B., REILLY, D., MCFARLAND, J. & RANJAN, D. 2017 Evaluation of turbulent mixing transition in a shock-driven variable-density flow. *J. Fluid Mech.* **831**, 779–825.

MOHAGHAR, M., CARTER, J., PATHIKONDA, G. & RANJAN, D. 2019 The transition to turbulence in shock-driven mixing: effects of Mach number and initial conditions. *J. Fluid Mech.* **871**, 595–635.

MOHAGHAR, M., MCFARLAND, J. & RANJAN, D. 2022 Three-dimensional simulations of reshocked inclined Richtmyer–Meshkov instability: effects of initial perturbations. *Phys. Rev. Fluids* **7**, 093902.

MORGAN, R.V., AURE, R., STOCKERO, J.D., GREENOUGH, J.A., CABOT, W., LIKHACHEV, O.A. & JACOBS, J.W. 2012 On the late-time growth of the two-dimensional Richtmyer–Meshkov instabilities in shock tube experiments. *J. Fluid Mech.* **712**, 354–383.

NIEDERHAUS, C.E. & JACOBS, J.W. 2003 Experimental study of the Richtmyer–Meshkov instability of incompressible fluids. *J. Fluid Mech.* **485**, 243–277.

OFER, D., ALON, U., SHVARTS, D., MCCRORY, R.L. & VERDON, C.P. 1996 Modal model for the nonlinear multimode Rayleigh–Taylor instability. *Phys. Plasmas* **3**, 3073–3090.

ORLICZ, G.C., BALASUBRAMANIAN, S. & PRESTRIDGE, K.P. 2013 Incident shock Mach number effects on Richtmyer–Meshkov mixing in a heavy gase layer. *Phys. Fluids* **25**, 114101.

ORON, D., ARAZI, L., KARTOON, D., RIKANATI, A., ALON, U. & SHVARTS, D. 2001 Dimensionality dependence of the Rayleigh–Taylor and Richtmyer–Meshkov instability late-time scaling laws. *Phys. Plasmas* **8**, 2883–2889.

PANDIAN, A., STELLINGWERF, R. & ABARZHI, S. 2017 Effect of a relative phase of waves constituting the initial perturbation and the wave interference on the dynamics of strong-shock-driven Richtmyer–Meshkov flows. *Phys. Rev. Fluids* **2**, 073903.

PLESSET, M.S. 1954 On the stability of fluid flows with spherical symmetry. *J. Appl. Phys.* **25**, 96–98.

RANJAN, D., NIEDERHAUS, J.H.J., OAKLEY, J.G., ANDERSON, M.H., BONAZZA, R. & GREENOUGH, J.A. 2008 Shock-bubble interactions: features of divergent shock-refraction geometry observed in experiments and simulations. *Phys. Fluids* **20**, 036101.

RAYLEIGH, L. 1883 Investigation of the character of the equilibrium of an incompressible heavy fluid of variable density. *Proc. Lond. Math. Soc.* **14**, 170–177.

RICHTMYER, R.D. 1960 Taylor instability in shock acceleration of compressible fluids. *Commun. Pure Appl. Maths* **13**, 297–319.

RIKANATI, A., ALON, U. & SHVARTS, D. 1998 Vortex model for the nonlinear evolution of the multimode Richtmyer–Meshkov instability at low Atwood numbers. *Phys. Rev.* E **58**, 7410–7418.

SADOT, O., EREZ, L., ALON, U., ORON, D., LEVIN, L.A., EREZ, G., BEN-DOR, G. & SHVARTS, D. 1998 Study of nonlinear evolution of single-mode and two-bubble interaction under Richtmyer–Meshkov instability. *Phys. Rev. Lett.* **80**, 1654–1657.

SAMULSKI, C., SRINIVASAN, B., MANUEL, M.J.-E., MASTI, R.L., SAUPPE, J.P. & KLINE, J. 2022 Deceleration-stage Rayleigh–Taylor growth in a background magnetic field studied in cylindrical and Cartesian geometries. *Matt. Radiat. Extrem.* **7**, 026902.

SHVARTS, D., ALON, U., OFER, D., MCCRORY, R. & VERDON, C. 1995 Nonlinear evolution of multimode Rayleigh–Taylor instability in two and three dimensions. *Phys. Plasmas* **2**, 2465–2472.

SOHN, S.I. 2003 Simple potential-flow model of Rayleigh–Taylor and Richtmyer–Meshkov instabilities for all density ratios. *Phys. Rev.* E **67**, 026301.

TAYLOR, G. 1950 The instability of liquid surfaces when accelerated in a direction perpendicular to their planes 1. *Proc. R. Soc. Lond.* **201**, 192–196.

VANDENBOOMGAERDE, M., SOUFFLAND, D., MARIANI, C., BIAMINO, L., JOURDAN, G. & HOUAS, L. 2014 An experimental and numerical investigation of the dependency on the initial conditions of the Richtmyer–Meshkov instability. *Phys. Fluids* **26**, 024109.

WANG, H., WANG, H., ZHAI, Z. & LUO, X. 2022 Effects of obstacles on shock-induced perturbation growth. *Phys. Fluids* **34**, 086112.

WANG, L.F., WU, J.F., GUO, H.Y., YE, W.H., LIU, J., ZHANG, W.Y. & HE, X.T. 2015 Weakly nonlinear Bell–Plesset effects for a uniformly converging cylinder. *Phys. Plasmas* **22**, 082702.

WOUCHUK, J.G. 2001 Growth rate of the linear Richtmyer–Meshkov instability when a shock is reflected. *Phys. Rev.* E **63**, 056303.

YANG, J., KUBOTA, T. & ZUKOSKI, E.E. 1993 Application of shock-induced mixing to supersonic combustion. *AIAA J.* **31**, 854–862.

ZHAI, Z., LIU, C., QIN, F., YANG, J. & LUO, X. 2010 Generation of cylindrical converging shock waves based on shock dynamics theory. *Phys. Fluids* **22**, 041701.

ZHAI, Z., ZHANG, F., ZHOU, Z., DING, J. & WEN, C. 2019 Numerical study on Rayleigh–Taylor effect on cylindrically converging Richtmyer–Meshkov instability. *Sci. China-Phys. Mech. Astron.* **62**, 124712.

ZHAN, D., LI, Z., YANG, J., ZHU, Y. & YANG, J. 2018 Note: a contraction channel design for planar shock wave enhancement. *Rev. Sci. Instrum.* **89**, 056104.

ZHANG, Q. & GUO, W. 2016 Universality of finger growth in two-dimensional Rayleigh–Taylor and Richtmyer–Meshkov instabilities with all density ratios. *J. Fluid Mech.* **786**, 47–61.

ZHANG, Q. & SOHN, S.I. 1996 An analytical nonlinear theory of Richtmyer–Meshkov instability. *Phys. Lett.* A **212**, 149–155.

ZHANG, Q. & SOHN, S.I. 1997 Nonlinear theory of unstable fluid mixing driven by shock wave. *Phys. Fluids* **9**, 1106–1124.

ZHOU, Z., DING, J., ZHAI, Z., CHENG, W. & LUO, X. 2020 Mode coupling in converging Richtmyer–Meshkov instability of dual-mode interface. *Acta Mechanica Sin.* **36**, 356–366.